



**AIAA 2002-5547**  
**SONIC BOOM REDUCTION USING**  
**AN ADJOINT METHOD FOR**  
**WING-BODY CONFIGURATIONS IN**  
**SUPERSONIC FLOW**

Siva K. Nadarajah , Antony Jameson and Juan J.  
Alonso

Department of Aeronautics and Astronautics  
Stanford University  
Stanford, California 94305 U.S.A.

**9th AIAA/ISSMO Symposium on**  
**Multidisciplinary Analysis and**  
**Optimization Conference**  
**September 4–6, 2002/Atlanta, GA**

# SONIC BOOM REDUCTION USING AN ADJOINT METHOD FOR WING-BODY CONFIGURATIONS IN SUPERSONIC FLOW

Siva K. Nadarajah\*, Antony Jameson† and Juan J. Alonso‡  
 Department of Aeronautics and Astronautics  
 Stanford University  
 Stanford, California 94305 U.S.A.

This paper presents an adjoint method for the calculation of remote sensitivities in supersonic flow. The goal is to develop a set of adjoint equations and their corresponding boundary conditions in order to quantify the influence of geometry modifications on the pressure distribution at an arbitrary location within the domain of interest. First, this paper presents the formulation and discretization of the adjoint equations. The special treatment of the adjoint boundary condition to obtain remote sensitivities is also discussed. Second, we present results that demonstrate the application of the theory to a three-dimensional remote inverse design problem using a low sweep biconvex wing and a supersonic business jet wing-body configuration.

## Introduction

The objective of this work is to develop the necessary methods and tools to facilitate the design of low sonic boom aircraft that can fly supersonically over land with negligible environmental impact. Traditional methods to reduce the sonic boom signature were targeted towards reducing aircraft weight, increasing lift-to-drag ratio, improving the specific fuel consumption, etc. Seebass and Argrow<sup>1</sup> revisited sonic boom minimization and provided a detailed study of sonic boom theory and figures of merit for the level of sonic booms.

Diverse methods have been employed in the design low-boom aircraft configurations. The following are a selected number of papers on this topic. Marconi et. al.<sup>2</sup> proposed a rather exotic concept to reduce the sonic boom. Their goal was to increase the apparent length of the aircraft by off-axis volume addition. A swept forward keel placed normal to the Mach plane increased the apparent length and proved to be effective in reducing the sonic boom strength. Komadina et. al.<sup>3</sup> evaluated twelve different configurations. The ground sonic boom signature, aircraft aerodynamics, mass properties, and flight performance were evaluated for all twelve configurations using em-

pirical methods. The two most promising concepts were then chosen and higher fidelity methods were used to compute the vehicle performance and characteristics. Farhat et. al.<sup>4</sup> argued that most sonic boom minimization techniques shape the aircraft's equivalent body of revolution in the vertical plane and not the true geometry to reduce the farfield pressure signatures. The authors used a combination of linearized and nonlinear aerodynamic theories, computational fluid dynamics based on the Euler equations, and a gradient based method to optimize the shape of the aircraft. The design variables were nose tilt angle and canard and wing dihedral, sweep, and twist angles.

In this paper the control theory approach is used to develop an automatic aerodynamic optimization method to reduce the sonic boom signature by computing the sensitivities of the near field pressure distribution. The adjoint equation can be derived using either a continuous or discrete approach. The discrete adjoint approach applies control theory directly to the discrete field equations. The discrete adjoint equation is then derived by collecting all the terms multiplied by the variation  $\delta w_{i,j}$  of the discrete flow variables. A detailed comparison of the continuous and discrete adjoint approaches was conducted by Nadarajah et al.<sup>5,6</sup>

Traditional adjoint implementations were aimed at reducing a cost function computed from the pressure distribution on the surface that is being modified. In this case, however, we would like to obtain sensitivity derivatives of pressure distributions that are not collocated at the points where the geometry is being

\*PhD Candidate, Student Member AIAA

†Thomas V. Jones Professor of Engineering, Stanford University, AIAA Fellow

‡Assistant Professor, Stanford University

Copyright © 2002 by the authors. Published by the American Institute of Aeronautics and Astronautics, Inc. with permission.

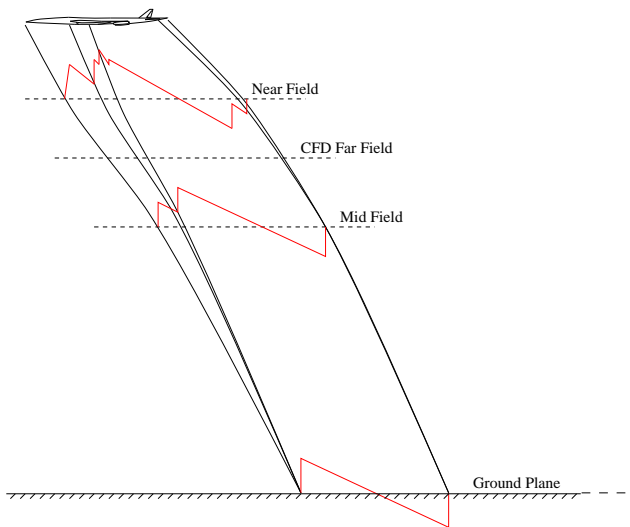


**Fig. 1 Schematic of Sonic Boom Minimization**

modified. This type of sensitivity calculation has only recently been attempted and will be necessary to solve sonic boom minimization problem. In order to consider the tailoring of the ground pressure signatures, it becomes necessary to compute sensitivity derivatives of the sonic boom signature with respect to a large number of design variables that affect the shape of the airfoil or aircraft.

For typical cruise altitudes required for aircraft efficiency, the distance from the source of the acoustic disturbance to the ground is typically greater than 50,000 ft. A reasonably accurate propagation of the pressure signature can only be obtained with small computational mesh spacings that would render the analysis of the problem intractable for even the largest parallel computers. An approach that has been used successfully in the past is the use of near to far field extrapolation of pressure signatures based on principles of geometrical acoustics and non-linear wave propagation. These methods are based on the solutions of simple ordinary differential equations for the propagation of the near field pressure signature to the ground.

Figure 1 is a schematic of the sonic boom minimization problem. ‘CFD Far Field’ indicates the far field boundary of the computational mesh. At a pre-specified distance below the aircraft and still within the CFD mesh, the location of a near field plane can be seen. This plane is the effective interface between the CFD solution and the wave propagation program. At the near field plane, the flow solution  $w_o$  is represented using a number of parameters,  $M$ , which can be taken as the number of mesh points on which the pressure waveform has a value different from the free stream.

The lower portion of the domain between the CFD near field and the ground plane is where the pressure signature propagation method will be active.

Given the conditions,  $w_o$ , the propagation altitude, and the altitude dependent atmospheric properties  $\rho(z), p(z), T(z)$ , the propagation method produces a flow solution at the ground plane we are interested in, which can be used to determine any of a variety of measures of sonic boom impact such as over-pressures, rise time, and impulse. This work focuses on controlling the near field signature which will be the input to the propagation program.

Through the support of the DARPA QSP Program, advanced algorithms for the design and optimization of quiet supersonic platforms have been developed at Stanford in the last year. Our experience has indicated that large reductions in the ground peak pressure cannot be achieved with minor shape modifications of the baseline configuration. Alternative design methods such as genetic algorithms have been used in a multi-level design environment to get in the neighborhood of the optimum design before switching over to a gradient-based method to refine the design. Promising results have been achieved by using genetic algorithms in a linear prediction environment. Once the ground peak pressure is at a desired level, then nonlinear methods using control theory were developed in order to meet several goals: first, to verify, if not improve, the results of the linear based method; second, to improve the design by using the remote inverse adjoint method; third, to allow the introduction of more objective functions to improve the final design.

The three papers surveyed at the beginning of this section share one common concept, that the sonic boom signature was reduced by modifying the current aircraft configuration. In Komadina et. al.<sup>3</sup> the authors evaluated a wide range of drastically different configurations. Marconi et. al.<sup>2</sup> added a swept keel and Farhat et. al.<sup>4</sup> used design variables that modified the nose tilt and wing and canard planform parameters. The remote inverse adjoint approach developed in this work modifies the true geometry not by altering its planform but its current shape grid point by grid point. Gradients are calculated for each point on the surface of the wing and fuselage and modifications are made based upon a simple steepest descent algorithm.

The adjoint approach to aerodynamic shape optimization has been under development at Stanford for the past several years through the generous support of the AFOSR. In this paper, a proof of concept of the remote inverse problem will be demonstrated in three dimensional supersonic flow. The possibility that the adjoint method could be adapted to solve the remote inverse problem was first demonstrated by Nadarajah et al.<sup>7</sup> for a two dimensional internal flow problem. Work on the remote inverse design of three-dimensional wings were demonstrated by Nadarajah et. al.<sup>8</sup>

## The Remote Inverse Design Problem using Control Theory

The aerodynamic properties that define the cost function are functions of the flow-field variables,  $w$ , and the physical location of the boundary, which may be represented by the function  $S$ .

Suppose that the performance is measured by a cost function

$$I = \varpi_1 \int_{\mathcal{B}_W} \mathcal{M}(w, S) d\mathcal{B}_\xi + \varpi_2 \int_{\mathcal{B}_{NF}} \mathcal{N}(w, S) d\mathcal{B}_\xi,$$

containing both wall boundary ( $\mathcal{B}_W$ ) and near field boundary ( $\mathcal{B}_{NF}$ ) contributions, where  $d\mathcal{B}_\xi$  includes the surface and near field elements in the computational domain, while  $\varpi_1$  and  $\varpi_2$  are the weighting coefficients. The coordinates  $\xi_i$  that describe the fixed computational domain are chosen so that each boundary conforms to a constant value of one of these coordinates. In general,  $\mathcal{M}$  and  $\mathcal{N}$  will depend on both the flow variables  $w$  and the metrics  $S$  defining the computational space.

The design problem is now treated as a control problem where the boundary shape represents the control function, which is chosen to minimize  $I$  subject to the constraints defined by the flow equations. A shape change produces a variation in the flow solution  $\delta w$  and the metrics  $\delta S$  which in turn produce a variation in the cost function

$$\delta I = \varpi_1 \int_{\mathcal{B}_W} \delta \mathcal{M}(w, S) d\mathcal{B}_\xi + \varpi_2 \int_{\mathcal{B}_{NF}} \delta \mathcal{N}(w, S) d\mathcal{B}_\xi, \quad (1)$$

with

$$\begin{aligned} \delta \mathcal{M} &= [\mathcal{M}_w]_I \delta w + \delta \mathcal{M}_{II}, \\ \delta \mathcal{N} &= [\mathcal{N}_w]_I \delta w + \delta \mathcal{N}_{II}, \end{aligned} \quad (2)$$

where we use the subscripts  $I$  and  $II$  to distinguish between the contributions associated with the variation of the flow solution  $\delta w$  and those associated with the metric variations  $\delta S$ . Thus  $[\mathcal{M}_w]_I$  and  $[\mathcal{N}_w]_I$  represent  $\frac{\partial \mathcal{M}}{\partial w}$  and  $\frac{\partial \mathcal{N}}{\partial w}$  with the metrics fixed, while  $\delta \mathcal{M}_{II}$  and  $\delta \mathcal{N}_{II}$  represent the contribution of the metric variations  $\delta S$  to  $\delta \mathcal{M}$  and  $\delta \mathcal{N}$  with the flow solution fixed.

The weak form of the Euler equations for steady flow is

$$\int_{\mathcal{D}} \frac{\partial \psi^T}{\partial \xi_i} \delta F_i d\mathcal{D} = \int_{\mathcal{B}} n_i \psi^T \delta F_i d\mathcal{B},$$

where the test vector  $\psi$  is an arbitrary differentiable function and  $n_i$  is the outward normal at the boundary. If a differentiable solution  $w$  is obtained to this equation, then it can be integrated by parts to give

$$\int_{\mathcal{D}} \psi^T \frac{\partial}{\partial \xi_i} \delta F_i d\mathcal{D} = 0. \quad (3)$$

Since this is true for any  $\psi$ , the differential form can be recovered. Here  $\delta F_i$  can be split into contributions

associated with  $\delta w$  and  $\delta S$  using a similar notation

$$\delta F_i = [F_{iw}]_I \delta w + \delta F_{iII} \quad \text{where, } [F_{iw}]_I = S_{ij} \frac{\partial f_j}{\partial w}.$$

The domain can then be split into two parts as shown in Figure 2. First, the near field domain ( $\mathcal{D}_1$ ) whose boundaries are the wing surface and the near field boundary plane. Second, the far field domain ( $\mathcal{D}_2$ ) which borders the near field domain along the near field boundary plane and the far field boundary.

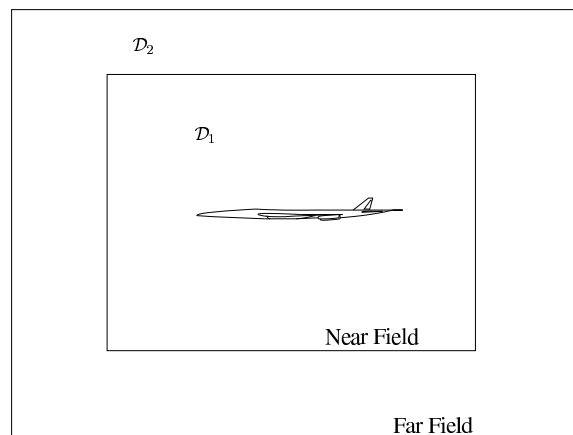


Fig. 2 Near Field and Far Field Domains

$$\int_{\mathcal{D}_1} \psi^T \frac{\partial}{\partial \xi_i} \delta F_i d\mathcal{D}_\xi + \int_{\mathcal{D}_2} \psi^T \frac{\partial}{\partial \xi_i} \delta F_i d\mathcal{D}_\xi = 0.$$

This may be integrated by parts to give

$$\begin{aligned} & \int_{\mathcal{B}_W} n_i \psi^T \delta F_i d\mathcal{B}_\xi - \int_{\mathcal{D}_1} \frac{\partial \psi^T}{\partial \xi_i} \delta F_i d\mathcal{D}_\xi \\ & + \int_{\mathcal{B}_{NF}} n_i (\psi^+ - \psi^-)^T \delta F_i d\mathcal{B}_\xi \\ & - \int_{\mathcal{D}_2} \frac{\partial \psi^T}{\partial \xi_i} \delta F_i d\mathcal{D}_\xi = 0, \end{aligned} \quad (4)$$

where  $\psi^+$  and  $\psi^-$  are the values of  $\psi$  above and below the boundary. Since the left hand expression equals zero, it may be subtracted from the variation in the cost function (1) to give

$$\begin{aligned} \delta I &= \int_{\mathcal{B}_W} [\varpi_1 \delta \mathcal{M} - n_i \psi^T \delta F_i] d\mathcal{B}_\xi \\ & + \int_{\mathcal{B}_{NF}} [\varpi_2 \delta \mathcal{N} - n_i (\psi^+ - \psi^-)^T \delta F_i] d\mathcal{B}_\xi \\ & + \int_{\mathcal{D}_1} \frac{\partial \psi^T}{\partial \xi_i} \delta F_i d\mathcal{D}_\xi + \int_{\mathcal{D}_2} \frac{\partial \psi^T}{\partial \xi_i} \delta F_i d\mathcal{D}_\xi. \end{aligned} \quad (5)$$

Now, since  $\psi$  is an arbitrary differentiable function, it may be chosen in such a way that  $\delta I$  no longer depends explicitly on the variation of the state vector  $\delta w$ . The gradient of the cost function can then be evaluated directly from the metric variations without

having to re-compute the variation  $\delta w$  resulting from the perturbation of each design variable.

Comparing equations (2) and (4), the variation  $\delta w$  may be eliminated from (5) by equating all field terms with subscript “ $I$ ” to produce a differential adjoint system governing  $\psi$

$$\left[ \frac{\partial \psi^T}{\partial \xi_i} [F_{iw}]_I \right]_{\mathcal{D}_1 + \mathcal{D}_2} = 0 \quad \text{in } \mathcal{D}. \quad (6)$$

The corresponding wall and near field adjoint boundary conditions are produced by equating the subscript “ $I$ ” boundary terms in equation (5) to produce

$$n_i \psi^T [F_{iw}]_I = \varpi_1 \mathcal{M}_w \quad \text{on } \mathcal{B}_W. \quad (7)$$

$$n_i (\psi^+ - \psi^-)^T [F_{iw}]_I = \varpi_2 \mathcal{N}_w \quad \text{on } \mathcal{B}_{NF}. \quad (8)$$

The boundary conditions satisfied by the flow equations restrict the form of the left hand side of the adjoint boundary conditions (7) and (8). Consequently, the boundary contribution to the cost functions  $\mathcal{M}$  and  $\mathcal{N}$  cannot be specified arbitrarily. Instead, it must be chosen from the class of functions which allow cancellation of all terms containing  $\delta w$  in the boundary integral of equation (5). The work in this paper uses a cell centered multigrid scheme with upwind-biased blended first-and-third-order fluxes for artificial dissipation, local time stepping, and implicit residual smoothing.

The remaining terms from equation (5) then yield a simplified expression for the variation of the cost function which defines the gradient

$$\begin{aligned} \delta I &= \int_{\mathcal{B}_W} \{ \varpi_1 \delta \mathcal{M}_{II} - n_i \psi^T [\delta F_i]_{II} \} d\mathcal{B}_\xi \\ &+ \int_{\mathcal{B}_{NF}} \{ \varpi_2 \delta \mathcal{N}_{II} - n_i (\psi^+ - \psi^-)^T [\delta F_i]_{II} \} d\mathcal{B}_\xi \\ &+ \int_{\mathcal{D}_1 + \mathcal{D}_2} \left\{ \frac{\partial \psi^T}{\partial \xi_i} [\delta F_i]_{II} \right\} d\mathcal{D}_\xi. \end{aligned} \quad (9)$$

The details of the formula for the gradient depend on the way in which the boundary shape is parameterized as a function of the design variables and the way in which the mesh is deformed as the boundary is modified. The inverse design boundary condition is applied to the near field, while sensitivity derivatives or the gradient are calculated on the airfoil surface. The gradient is obtained by perturbing each point on the lower wall. Once the gradient  $\mathcal{G} = \frac{\partial I}{\partial b}$  has been determined, it can be used to drive a variety of gradient-based search procedures. The search procedure used in this work is a descent method in which small steps are taken in the negative gradient direction. Let  $\mathcal{F}$  represent the design variable and  $\mathcal{G}$  the gradient.

However, it is better to replace the gradient  $\mathcal{G}$  by a smoothed value  $\bar{\mathcal{G}}$  in the descent process. This acts as a preconditioner which allows the use of much larger steps and ensures that each new shape in the optimization sequence remains smooth.

## Implementation of Remote Inverse Design

The development of a multiblock code for the design method entails three separate parts: the solution of the flow equations, the solution of the adjoint equations, and the calculation of the gradient integral formulas. Both the flow and adjoint solutions are obtained using a finite volume discretization of the governing equations with the flow and adjoint variables stored at cell centers. Similarities between the flow and adjoint equations allow them to be solved using exactly the same efficient numerical scheme, with the exception of the of the boundary conditions, where in the case of the adjoint equation, the boundary condition appears as source terms and are added to the adjoint fluxes. Therefore, the same domain decomposition is used for the flow and adjoint solvers.

The three-dimensional C-H meshes for the wing and wing-body were generated using a conformal mapping transformation method. Flows were computed on  $n_i \times n_j \times n_k = 193 \times 49 \times 33$  meshes. The domain was decomposed into subdomains containing  $\frac{n_i}{N_{p_i}} \times \frac{n_j}{N_{p_j}} \times \frac{n_k}{N_{p_k}}$  points, where  $N_{p_i}$ ,  $N_{p_j}$ , and  $N_{p_k}$  are the number of subdomains in the  $i, j$ , and  $k$  coordinate directions. The number of subdomains in each coordinate direction is an input into the program. It must also be mentioned that the number of subdomains in each coordinate direction limits the number of maximum number of multigrid levels that can be used. This limits the convergence rate of the multiblock code. Domains were decomposed such that at least four multigrid levels were possible in each subdomain. Communication between subdomains is performed through halo cells surrounding each subdomain boundary. Since both the convective and dissipative fluxes are calculated at the cell faces, all six neighboring cells are needed to compute the convective flux through the face and twelve cells are needed for the dissipative flux which uses blended first and third order differences.

The design procedure is as follows. First, the flow solver module is run until at least 5 orders of magnitude drop in the residual have been obtained. Second, the cost function is calculated and the location of the source terms are determined. Third, the adjoint solver is run until at least 4 orders of magnitude drop in the residual. Next, the gradient is calculated by perturbing each point on the wing surface mesh. The resulting gradient is then smoothed by an implicit smoothing technique. Then the wing and body geometry is updated and the grid is modified. The entire process is repeated until the conditions for optimality are satisfied. At each subsequent design iteration, 20 multigrid cycles for the flow and adjoint solver are used before the gradient is calculated. Figure 3 illustrates the design procedure.

Figure 4 shows the location of the near field pressure

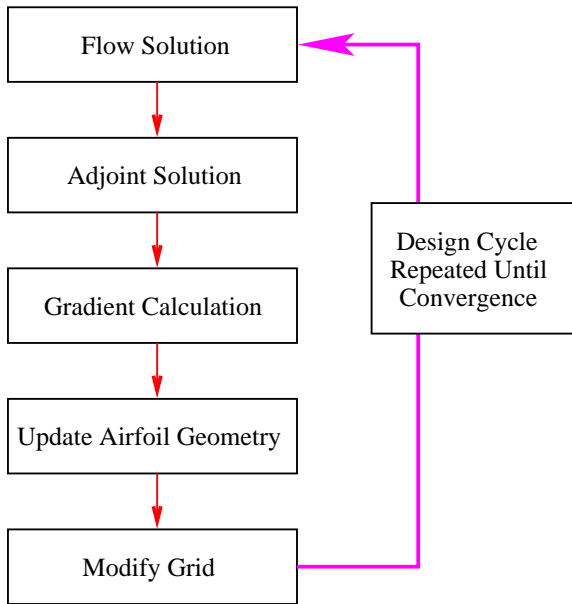


Fig. 3 Design Procedure

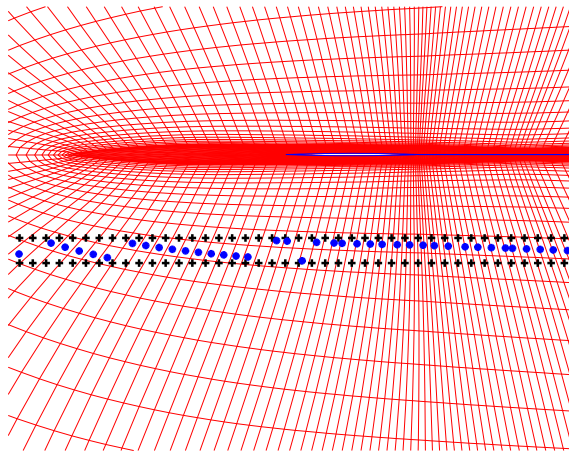


Fig. 4 Location of Near Field Pressure and Adjoint Remote Sensitivity Source Terms

(+) and the adjoint remote sensitivity source terms (o). The variation of the cost function is first calculated by taking the difference between the current and target near field pressures at the (+)s for every  $z$ -plane. A search algorithm then seeks for centers of cells that are within the cube defined by the (+) points. The search algorithm is repeated at every design cycle, since the possibility exists that the mesh may have modified and thus requiring a new location for the source term. The source terms are then computed using a trilinear interpolation at this location.

An alternative method for problems with more than one objective function is to develop separate adjoint equations, one for each objective function. Both gradients are then calculated separately, multiplied by weights, and summed. A direction of improvement is then achieved with the new gradient. This method has the advantage that the user is better equipped

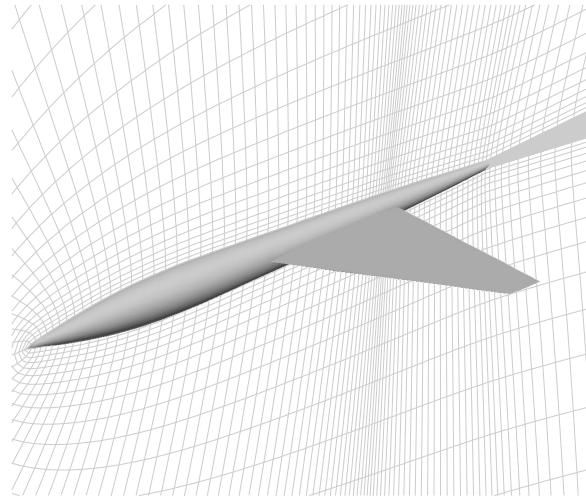


Fig. 5 Business Jet Wing-Body Configuration: Biconvex Wing, 193x49x33 C-H Grid, 8 Blocks

with knowledge regarding the difference in magnitude between the two gradients. Appropriate weights can then be chosen to achieve the desired compromise. A disadvantage is the need to calculate a separate adjoint solution for each objective function.

In this work, we preferred to use a composite cost function, since we had apriori knowledge regarding the magnitude of the gradient contribution from the remote inverse cost function and the drag minimization cost function.

## Results

This section presents the results of remote inverse and drag minimization for three dimensional wings and wing-body configurations in supersonic flow. The objective is to reduce the peak pressure at the near field plane and thus reduce the ground signature peak. Viscous effects are likely to be very small in these examples, so it is sufficient to use the Euler equations. The calculations were performed with a new SYN88-MBC multiblock code that takes advantage of the FORTRAN 90/95 derived data type architecture. The flow solver is augmented with an adjoint solver and shape modification routines to allow automatic shape optimization.

### Wing-Body Configuration: Sonic Boom Reduction, Without Lift Constraint, Wing Redesign

The wing-body supersonic business jet configuration was sized to accommodate between 6 to 8 passengers with a gross take-off weight of 100,000 lbs and a fuselage length of 100 feet. The supersonic flight condition at which all designs were calculated is Mach 1.5. Figure 5 shows the wing-body configuration. The fuselage is cylindrical and the maximum diameter occurs at 31% measured from the nose of the fuselage. The wing is a biconvex wing with a  $7.125^\circ$  leading edge sweep, an aspect ratio of 3.0, and a taper ratio of 0.218.

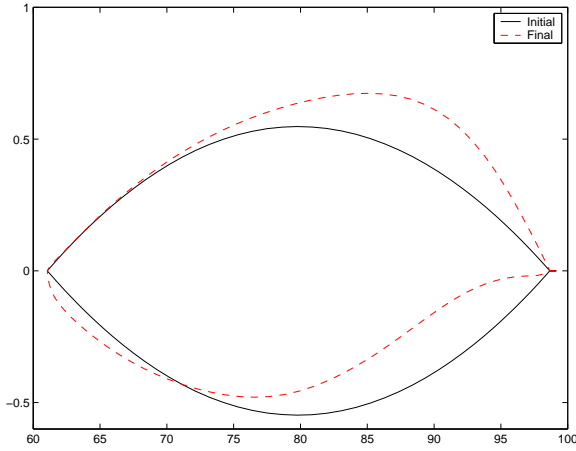


Fig. 6 Initial and Final Root Airfoils at  $M_\infty = 1.5$

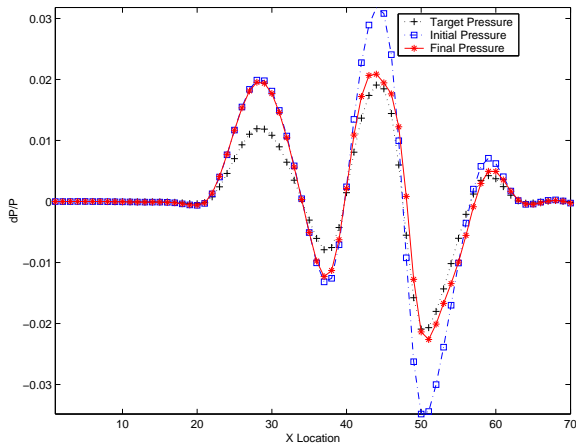


Fig. 7 Sonic Boom Reduction: Target, Initial, and Final Near Field Pressure Distribution after 50 Design Cycles.  $M_\infty = 1.5$ ,  $\alpha = 1.62^\circ$ , Lift Not Constrained

The root airfoil is a 3% thick biconvex airfoil and the tip is 1.5%. The biconvex profile in the center sections was obtained by interpolating between the root and tip. The airfoils were constructed to accommodate thick spars at the 10% and 80% chord locations. The baseline wing does not have geometric twist. The computational mesh has eight blocks with 193x49x33 nodes on a C-H grid. The fuselage has 25 points in the cross-streamwise-direction and 144 points in the streamwise-direction. The wing contains 97 points in the streamwise-direction and 17 sectional cuts in the spanwise-direction.

In order to illustrate the possibility of sonic boom reduction, a target pressure distribution was obtained by re-scaling the initial near field pressure distribution. Ultimately, this step will be replaced by a method that produces a target near field pressure based upon the desired ground pressure signature. The target pressure was obtained using the new SYN88-MBC (Multiblock) code at a flight condition of  $M_\infty = 1.5$ . The target pressure is then reduced by 40% of its original value.

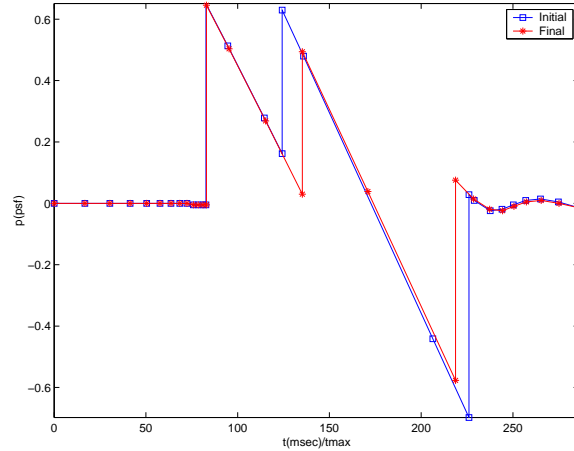


Fig. 8 Sonic Boom Reduction: Initial and Final Ground Signatures after 50 Design Cycles.  $M_\infty = 1.5$ ,  $\alpha = 0^\circ$ , Lift Not Constrained

The objective function is the integral of the difference between the current and target near field pressures. The wing thickness is constrained. To maintain the wing thickness distribution the upper surface profile is modified to allow spar locations at the 10% and 80% chord locations. At the end of each design cycle the minimum permissible thickness constraint is imposed at each chordwise cut between the 10% and 80% chord locations. Points from the leading edge upto the 10% chord location and from the 80% chord location to the trailing edge are not constrained and free to move in any direction. The lift coefficient in this case is not constrained. In this design, the design variables are only the points on the surface of the wing. Therefore only the second peak in the near field pressure profile will be expected to change. The flow is calculated at Mach 1.5 at a fixed angle of attack of  $1.62^\circ$ .

Figure 6 illustrates the initial and final root airfoil profiles. The lower surface of the final airfoil contains a slightly larger expansion region when compared with the original biconvex airfoil. It is this modification that allows the near field wing peak pressure (second peak) to be reduced. The larger expansion region weakens the strength of the leading edge attached shock in the near field region. Figure 7 shows the initial near field pressure in blue ( $\square$ ) and the target pressure in black ( $+$ ). After 50 design cycles, the final near field pressure distribution is obtained and illustrated as the red ( $*$ ) line. The wing peak pressure has been reduced by 40%.

The large modifications on the wing upper surface is a result of the thickness constraint. Since the lift coefficient was not constrained,  $C_L$  reduced from 0.1 to 0.073. The baseline wing drag coefficient is 0.00568 and the final wing drag increased to 0.00582. Even if drag due to lift has decreased due to the decrease in the lift coefficient, but the stronger attached leading edge shock has increased the wing wave drag.

The complete shape optimization procedure for

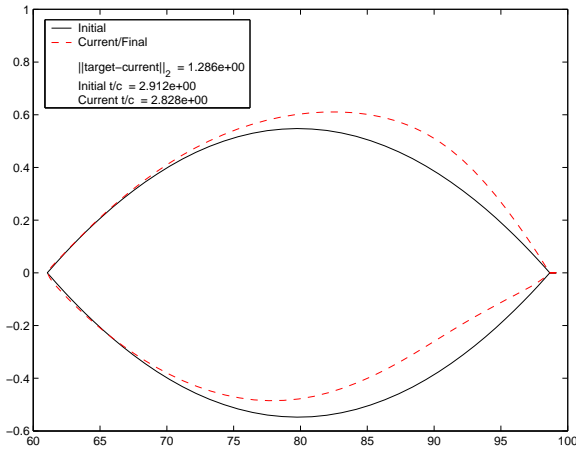


Fig. 9 Initial and Final Root Airfoils at  $M_\infty = 1.5$

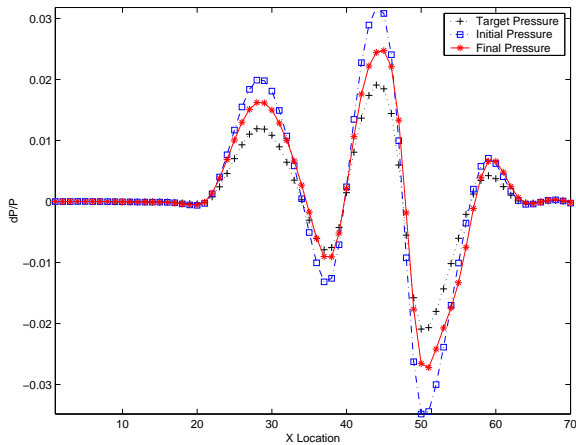


Fig. 10 Sonic Boom Reduction: Target, Initial, and Final Near Field Pressure Distribution after 50 Design Cycles.  $M_\infty = 1.5$ ,  $\alpha = 2.39^\circ$ ,  $C_L = 0.1$

sonic boom reduction requires the determination of desirable ground boom signatures. In figure 8 we show the initial and final ground signature profiles. The PC Boom software for far field propagation developed by Wyle Associates was used to calculate the ground signatures.

### Wing-Body Configuration: Sonic Boom Reduction, Lift Constraint

We now repeat the same design case but with the following three changes: First, the lift coefficient is constrained at 0.1. Second, gradients are calculated for points on the surface of the fuselage and thus allowed to be modified. Third, the objective function is a weighted sum of the drag coefficient and integral of the difference between the current and target near field pressures, where  $\varpi_1$  is the weight on the drag coefficient and  $\varpi_2$  is the weight on the remote inverse cost function. In this case, the drag coefficient weight is,  $\varpi_1 = 0.005$  and the remote inverse cost function weight is set to  $\varpi_2 = 1$ .

The value of the lift coefficient is maintained by ad-

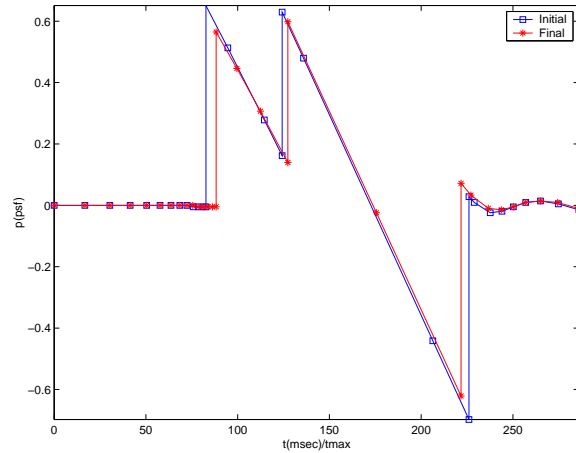


Fig. 11 Sonic Boom Reduction: Initial and Final Ground Signatures after 50 Design Cycles.  $M_\infty = 1.5$ ,  $\alpha = 2.39^\circ$ ,  $C_L = 0.1$

justing the angle of attack to attain the desired lift coefficient of 0.1. Thickness ratio at each span station is forced to remain the same.

Figure 9 illustrates the baseline and optimized airfoil. Figure 10 shows the target, initial, and final near field pressure distributions. The desired target pressure distribution is not achieved in contrast to the unconstrained case illustrated in Figure 7. In this case, there is a struggle between the near field peak pressure reduction versus maintenance of constant lift. Each design cycle, produces a shape modification that shifts the near field pressure distribution towards the target pressure. Unfortunately, this also causes a reduction in the lift coefficient. This must be compensated by an increase in the angle of attack to maintain the total lift coefficient, which in turn leads to an increase in the near field peak pressure. After 50 design cycles, the solution converges to the (\*) line in Figure 10. The final fuselage peak pressure has been reduced to almost 18% its original value and the wing peak pressure reduced by 22%.

In order to maintain the lift coefficient, the angle of attack was increased from  $1.62^\circ$  to  $2.39^\circ$ . The wing drag increased from 0.00568 to 0.00574. In an alternate test case, where the drag coefficient weight was set to zero, the near field peak pressure for both the fuselage and wing were reduced by 18% and 25%, however, the wing drag coefficient increased to 0.00610. Table 1 contains a comparison of the two design cases. It clearly shows that a cost function that does not include the drag coefficient will result to larger reductions in the wing near field peak pressure. However, in a multidisciplinary design environment, its critical that other important parameters are kept within acceptable amounts and a trade-off between the various design goals are met. The table clearly shows that a composite cost function that includes the drag coefficient was unable to reduce both the near field peak pressure and drag coefficient but it was able to re-

duce the peak pressure while maintaining the wing drag coefficient. A more detail study of the effect of the weights on the cost functions were presented by Nadarajah et. al.<sup>8</sup> at the Aerospace Sciences Meeting at Reno.

Case	Fuselage Peak Reduction	Wing Peak Reduction	Wing $C_D$
Baseline			0.00568
Remote Inverse	18%	25%	0.00610
Drag and Remote Inverse	18%	22%	0.00574

**Table 1 Near Field Peak Pressure Reduction and Wing Drag Coefficient for Various Design Cases**

In figures 12 and 13 the initial and final pressure contours are plotted. The majority of the changes in the shape localized around the lower surface wing-fuselage intersection. The larger expansion regions on the lower surface of the wing is illustrated in these plots by the shorter red region (compression) and the longer green-orange region. Figure 14 illustrates the initial fuselage mesh. In figure 15 we show the final fuselage mesh. The larger expansion region on the underside of the fuselage around the wing-fuselage intersection is clearly due to the increase in the fuselage curvature.

## Conclusions

The results demonstrate the feasibility of remote inverse calculations using the adjoint method. An application to the sonic boom minimization resulted in an 40% reduction in the near field peak pressure for the unconstrained biconvex wing. In the constrained problem, the fuselage peak pressure reduced by 18% and the wing peak reduced by 22%. It proved highly beneficial to use a composite cost function consisting of the sum of the weighted remote inverse and drag minimization cost functions, resulting in final designs that had a reduction in the peak pressure while maintaining constant wave drag. Cases with no drag coefficient added to the integral of the near field pressure difference in the objective function saw an increase in the drag coefficient.

## Acknowledgments

This research has benefited greatly from the generous support of the AFOSR under grant number AF F49620-98-1-022 and DARPA QSP Program under grant number MDA972-01-2-0003.

## References

- <sup>1</sup>R. Seebass, B. Argrow. *Sonic Boom Minimization Revisited*. *AIAA paper 98-2956*, AIAA 2nd Theoretical Fluid Mechanics Meeting, Albuquerque, NM, June 1998.
- <sup>2</sup>F. Marconi, R. Bowersox, M. Orr, J. Mozingo, and J. Schetz *Sonic Boom Alleviation using Keel Configurations* *AIAA 2002-0149*, 40th Aerospace Sciences Meeting and Exhibit, Reno, Nevada, January 2002.

<sup>3</sup>S. Komadina, A. Drake, and S. Bruner *Development of a Quiet Supersonic Aircraft with Technology Applications to Military and Civil Aircraft*. *AIAA 2002-0519*, 40th Aerospace Sciences Meeting and Exhibit, Reno, Nevada, January 2002.

<sup>4</sup>C. Farhat, K. Maute, B. Argrow, and M. Nikbay *A Shape Optimization Methodology for Reducing the Sonic Boom Initial Pressure Rise*. *AIAA 2002-0145*, 40th Aerospace Sciences Meeting and Exhibit, Reno, Nevada, January 2002.

<sup>5</sup>S. Nadarajah and A. Jameson. *A Comparison of the Continuous and Discrete Adjoint Approach to Automatic Aerodynamic Optimization*. *AIAA 00-0667*, AIAA 38th. Aerospace Sciences Meeting and Exhibit, Reno, NV, January 2000.

<sup>6</sup>S. Nadarajah and A. Jameson. *Studies of the Continuous and Discrete Adjoint Approaches to Viscous Automatic Aerodynamic Shape Optimization* *AIAA 2001-2530*, AIAA 15th. Computational Fluid Dynamic Conference, Anaheim, Ca, June 11-14, 2001.

<sup>7</sup>S. Nadarajah, A. Jameson, J. Alonso. *An Adjoint Method for the Calculation of Non-Collocated Sensitivities in Supersonic Flow*. In *Proceedings of First MIT Conference on Computational Fluid and Solid Mechanics*, June 12-15, 2001.

<sup>8</sup>S. Nadarajah, A. Jameson., and J. Alonso *An Adjoint Method for the Calculation of Remote Sensitivities in Supersonic Flow*. *AIAA 2002-0261*, AIAA 40th. Aerospace Sciences Meeting and Exhibit, Reno, NV, January 2002.

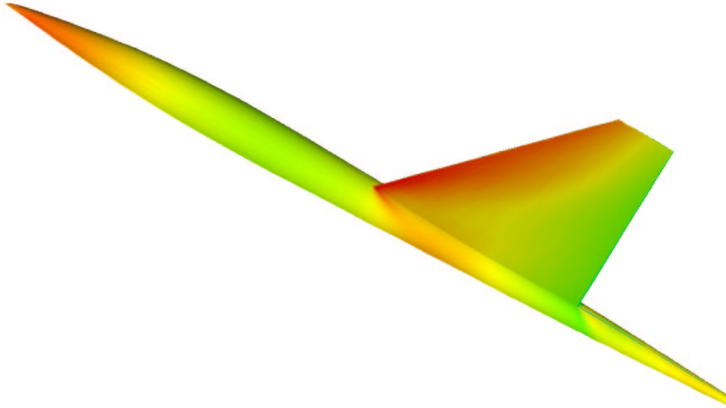


Fig. 12 Initial Pressure Contour at  $M_\infty = 1.5$

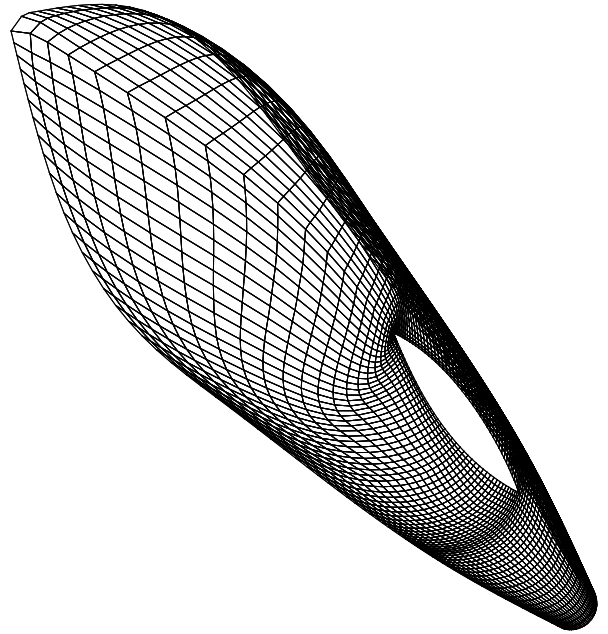


Fig. 14 Initial Fuselage Mesh

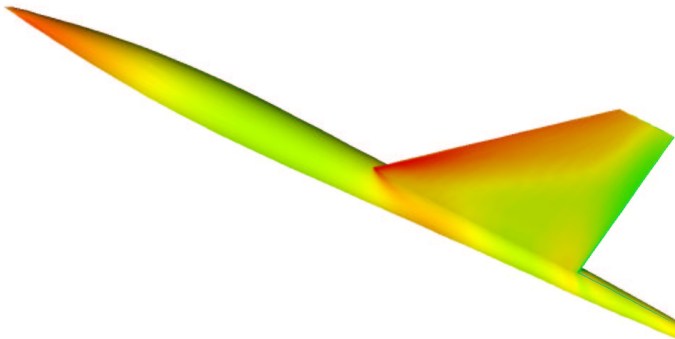


Fig. 13 Final Pressure Contour at  $M_\infty = 1.5$

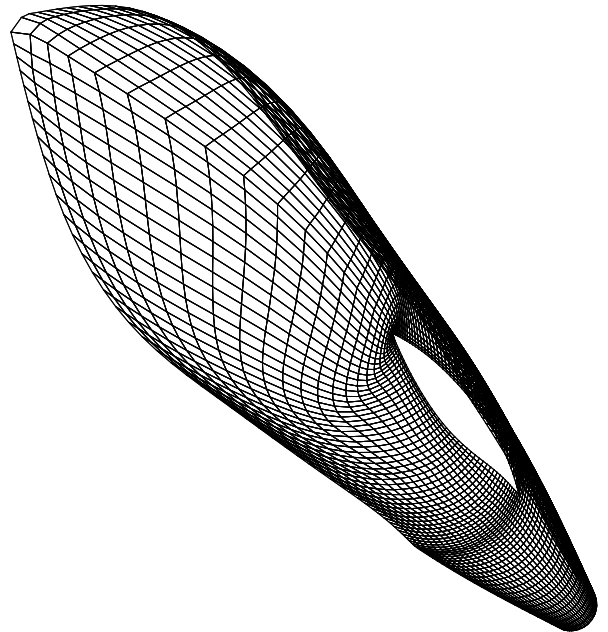


Fig. 15 Final Fuselage Mesh